Journal of Materials Chemistry A

ROYAL SOCIETY OF CHEMISTRY

PAPER

View Article Online
View Journal | View Issue

Check for updates

Cite this: J. Mater. Chem. A, 2025, 13, 28284

Tailoring plasmonic coupling in black gold-decorated porous polymer membranes *via all-in-one* synthesis for enhanced photocatalytic peroxymonosulfate activation

Janine Gerlach,[a] Nourman Barakat[a] and Lukas Fischer *[abc]

Advanced oxidation processes (AOPs) employing heterogeneous metal catalysts offer promise for degrading persistent organic pollutants in water, but often suffer from low process efficiency, catalyst instability, and recovery challenges. Here, we report an "*all-in-one*" strategy combining *in situ* synthesis of gold nanoparticles (AuNPs) in a polyethersulfone (PES) casting solution with their simultaneous immobilization within porous PES membranes *via* film casting *cum* phase separation. Crucially, all used $KAuCl_4$ precursor was fully converted and subsequently incorporated into the membrane matrix as AuNPs, yielding near-perfect material effciency. By copper doping, varying reductant ($NaBH_4$) concentration, and polyvinylpyrrolidone (PVP) capping, we could precisely control effective size (5, 12, 26 or 51 nm) and spatial arrangement of AuNPs within the membranes. Notably, PVP capping promoted immobilization of AuNPs as well-dispersed nanoclusters with tailored plasmonic coupling, resulting in broadband black plasmonic visible-light absorption (7.5–3.0% reflectance, 400–800 nm). The gold-decorated membranes were evaluated for photocatalytic activation of peroxymonosulfate (PMS) in the flow-through oxidation of ofloxacin (OFL) in water. The black gold membrane exhibited significant visible-light enhancement (70% rate increase), achieving the highest OFL degradation rate (194 μg OFL per mg catalyst per h). Mechanistic studies suggested a dual gold catalysis pathway: surface-mediated non-radical PMS activation in the dark and plasmonic photocatalytic generation of superoxide radicals ($^{\bullet}O^{2-}$) under illumination. In continuous flow-through operation, the black gold membrane achieved >99% OFL (0.75 mg L^{-1}) removal at short residence times (~3.5 s), even in a complex wastewater ion matrix. It further mantained high stability over 12 h of operation without performance loss or gold leaching.

Received 22nd April 2025
Accepted 26th July 2025

DOI: 10.1039/d5ta03185k

rsc.li/materials-a

Open Access Article. Published on 28 July 2025. Downloaded on 4/4/2026 4:36:24 PM.
This article is licensed under a Creative Commons Attribution 3.0 Unported Licence.

1 Introduction

Global water resources are increasingly threatened by pollution from anthropogenic sources, posing a pressing environmental challenge. For instance, the widespread contamination of aquatic environments with antibiotics promotes the proliferation of antibiotic-resistant bacteria.[1–4] Conventional wastewater treatment plants (WWTPs) are currently ineffective at removing such micropollutants, resulting in their accumulation in natural water bodies.[5,6] Advanced oxidation processes (AOPs) offer a promising solution by generating highly reactive active species from oxidants, which are capable of degrading a wide range of organic contaminants.[7] However, commercial adoption of AOPs for water treatment has been hampered by long treatment times and high operational costs.[8]

The treatment capacity of AOPs can be significantly enhanced by employing heterogeneous metal catalysts to activate oxidants, such as peroxymonosulfate (HSO_5^-) or hydrogen peroxide (H_2O_2).[9,10] However, state-of-the-art metal catalysts face significant limitations. First, many transition metals exhibit poor stability under the oxidative conditions of AOPs, leading to metal ion leaching during operation.[11–14] This leaching diminishes catalytic efficiency, compromises long-term stability, and introduces secondary metal pollution. Noble metal catalysts (*e.g.*, gold) offer superior stability but present different challenges. Their high redox potentials typically hinder the M(X)/M(X + 1) redox cycles common in transition metals, often leading to lower intrinsic activity for activating oxidants.[15] Consequently, noble metals favour non-radical pathways or direct electron transfer mechanisms rather than radical generation.[16] Furthermore, while photocatalysis using semiconductor materials (like transition metal oxides) is established, leveraging the localized surface plasmon

[a]Lehrstuhl für Technische Chemie II, University Duisburg-Essen, Universitätsstr. 7, 45141 Essen, Germany. E-mail: Lukas.Fischer@uni-due.de
[b]Center for Water and Environmental Research (ZWU), University Duisburg-Essen, Universitätsstr. 2, 45141 Essen, Germany
[c]Center for Nanointegration Duisburg-Essen (CENIDE), University Duisburg-Essen, Carl-Benz-Str. 199, 47057 Duisburg, Germany

This journal is © The Royal Society of Chemistry 2025

Open Access Article. Published on 28 July 2025. Downloaded on 4/4/2026 4:36:24 PM. This article is licensed under a Creative Commons Attribution 3.0 Unported Licence.

resonance (LSPR) of noble metals like gold for "standalone" photocatalysis (*e.g.*, without heterojunction to a semiconductor) in water treatment is mostly unexplored.[17,18]

A second challenge stems from the prevalent use of catalysts in powder form, which complicates recovery and is poorly suited for continuous flow-through water treatment systems.[19–21] Immobilizing catalysts within porous polymer membranes offers a promising solution for achieving continuous processes.[22,23] These membranes are commonly fabricated *via* liquid non-solvent induced phase separation (NIPS).[24] In NIPS, a polymer dissolved in a suitable solvent (the casting solution) is cast as a thin film and immersed in a non-solvent bath (typically water).[25] Solvent/non-solvent exchange triggers polymer precipitation, forming a porous membrane structure.[26] Conventional methods for incorporating catalysts include blending pre-synthesized metal nanoparticle powders into the casting solution or coating metals onto pre-formed membranes.[27–30] The pre-synthesis of nanoparticles for blending approaches often leads to significant material loss during powder isolation and is plagued by particle agglomeration. This is especially true for noble metals like gold, which are prone to irreversible sintering.[31] As a result, blending often yields membranes with poor catalyst accessibility.[32,33] Coating methods, which involve immersing the membrane in metal precursor solutions for *in situ* reduction/solidification, typically suffer from even lower material efficiency.[34–37] Only a small fraction of the metal precursor usually deposits as solid particles onto the membrane, and these particles can readily detach as they are bound solely by adsorption. This inefficient material usage is especially detrimental when employing scarce and expensive noble metals.

To address these challenges, we report a material-efficient, *all-in-one* synthesis of porous polyethersulfone (PES) membranes decorated with gold nanoparticles (AuNPs). Adapted from methods we recently developed,[38–40] this process integrates the *in situ* sonochemical reduction of $KAuCl_4$ to form AuNPs directly within the PES casting solution, followed immediately by membrane fabrication *via* NIPS. Crucially, we demonstrate a strategy to control the size and spatial arrangement of the immobilized AuNPs, thereby tuning their collective plasmonic properties for enhanced light absorption. We show that the resulting membranes, featuring tailored plasmonic AuNPs, efficiently activate peroxymonosulfate (PMS) in the visible-light-enhanced photocatalytic degradation of ofloxacin (OFL) in water. Furthermore, we elucidate the underlying catalytic mechanism and demonstrate the high performance and stability of these membranes in continuous flow-through water treatment.

2 Materials and methods

2.1 Materials

All materials are listed in Section S1 of the SI.

2.2 *All-in-one* synthesis of gold-decorated membranes

150 mg PES, 20 mg $KAuCl_4$, 0.7 or 0 mg $CuCl_2$ and 10 or 0 mg polyvinylpyrrolidone (PVP) were dissolved in 850 mg *N*-methyl-2-pyrrolidone (NMP)/dimethyl sulfoxide (DMSO) (70/30). Afterward, a certain mol eq. $NaBH_4$ (relative to metal) and 50 mg ethanol were added to this casting solution under high-shear mixing (neoLab 72 020 vortex mixer at 3150 rpm). Then, the *in situ* metal reduction was conducted in the casting solution for 1 h under constant ultrasonication in a sonication bath at 30 °C, 45 kHz and 100 W (Transonic TI-H-10 from Elma). Finally, the casting solution was degassed for 15 min in a vacuum oven at 50 °C and 50 mbar.

Directly afterwards, the casting solution was used for film casting on a glass plate with a film thickness of 200 μm and at a casting speed of 10 mm s^{-1} (at room-temperature of ~22 °C and at ~30% humidity). After casting, the film was immersed in a deionized (DI) water precipitation bath at room-temperature.

After fabrication, the final gold-decorated membranes were stored in fresh DI water.

2.3 Material characterization

Two 16 mm samples of each membrane were weighted, and their thickness was determined, both in water-wet and dry state. From this data, their porosity (water-accessible pore volume) was calculated.

For scanning electron microscopy (SEM) and energy-dispersive X-ray spectroscopy (EDX), membrane samples were dried and then frozen in liquid nitrogen, followed by braking to access the cross-section and sputter coating with Pt. SEM and EDX were conducted on an Apreo S LoVac system from Thermo Fisher Scientific at a pressure of 10^{-3} Pa, an accelerating voltage of 5 kV (SEM) or 20 kV (EDX), and a current of 13 Pa.

For dynamic light scattering (DLS) analysis, a 14 mm coupon of each gold-decorated membrane was dried and then dissolved in 5 mL NMP (shaking for 20 min). The dispersion was analysed (90 s measurement time) using a NANO-flex® 180° DLS system from Particle Metrix GmbH. Afterward, the UV-Vis extinction of that same dispersion was measured between 400–800 nm using a Cary UV-Vis spectrophotometer from Varian.

The relative diffuse reflectance (compared to barium sulfate) of the membranes was determined in the wavelength range from 400 to 800 nm *via* the integrating sphere method using a UV-2600i system from Shimadzu.

2.4 Catalytic OFL oxidation *via* PMS activation

All batch reactions were conducted with 16 mm membrane coupons immersed in 10 mL reaction solution. The reactions were carried out under constant shaking and at a temperature of 30 °C using a heated shaker plate (Titramax 1000 from Heidolph). The reactions were stopped after 2 h by removing the membrane coupons from the solution, directly followed by analysis of the reaction solution using a Cary UV-Vis spectrophotometer from Varian (see SI, Section S2). Each batch reaction was conducted twice with two different samples of each membrane.

All reactions in flow-through mode were conducted by placing membrane coupons into a transparent dead-end membrane module with a 3 cm^2 active area (reusable polycarbonate filter holder from Sartorius). The membrane module

Open Access Article. Published on 28 July 2025. Downloaded on 4/4/2026 4:36:24 PM. This article is licensed under a Creative Commons Attribution 3.0 Unported Licence.

was connected to a peristaltic pump, which supplied the feed solution at a constant flow rate. The membrane module was placed inside a closed chamber (see SI, Section S3), approximately 10 cm below the visible-light source (OSRAM LED PAR16 4.2 W spotlight). To start the experiment, the feed was connected to the peristaltic pump, and, for photocatalytic experiments, the visible-light source was turned on. Immediately after collecting each permeate sample, it was analysed using a Cary UV-Vis spectrophotometer from Varian (see SI, Section S2).

3 Results and discussion

3.1 *All-in-one*: particle synthesis and membrane preparation

We recently introduced an *all-in-one* approach for preparing membranes with immobilized transition metal nanoparticles.[38–40] In this work, we adapted and extended this method to synthesize porous polyethersulfone (PES) membranes decorated with AuNPs, specifically focusing on tuning nanoparticle size and inter-particle spacing to control their collective plasmonic properties for enhanced catalysis (Fig. 1).

The process started with the *in situ* sonochemical synthesis of zerovalent AuNPs from $AuCl_4^-$ with $NaBH_4$ directly within the PES (15 wt%) casting solution (NMP/DMSO 70 : 30). Critically, ethanol served as quencher for excess $NaBH_4$ *via* ethanolysis, a reaction catalyzed by the *in situ* formed AuNPs (see schematic in Fig. 1). Immediately after nanoparticle formation, the casting solution containing the suspended AuNPs was cast into a thin film and immersed in a water bath to induce phase separation of the matrix polymer (PES), forming the porous membrane (see Section 2.2). This integrated approach offers two key advantages: (1) it immobilizes the nanoparticles in the membrane matrix directly after their formation, effectively 'freezing' their size and dispersion state achieved in solution. (2) It ensures high material efficiency, as the elimination of intermediate purification and handling steps mitigates the metal loss associated with traditional powder catalyst synthesis.

3.2 Basic membrane characterization

This *all-in-one* method was employed to prepare membranes decorated with gold-only (Au_{10Red}) and copper-doped (3 wt% of gold) AuNPs ($AuCu_{10Red}$), both synthesized using 10 mol equivalents (eq.) of $NaBH_4$ (relative to total metal precursor).

To investigate the effect of reductant concentration on nanoparticle properties, Cu-doped Au membranes were also prepared using 3 eq. ($AuCu_{3Red}$) and 1.5 eq. ($AuCu_{1.5Red}$) of $NaBH_4$. Furthermore, PVP was used as a capping agent during the *in situ* synthesis with 3 eq. $NaBH_4$ ($AuCuPVP_{3Red}$). Notably, both the Cu-doping and PVP capping of AuNPs was realized by simply adding Cu^{2+} and/or PVP with $AuCl_4^-$ to the casting solution. Analysis of the casting solutions also revealed that >99% of the metal precursors were reduced by $NaBH_4$ after 1 h reaction under all conditions (see SI, Section S4), confirming the effectiveness of the *in situ* particle synthesis.

Although cast with a doctor blade set to 200 μm, the final dry membrane thicknesses ranged from approximately 90 to 110 μm (Table 1). This thinning compared to the initial wet thickness is typical for the employed NIPS process, resulting from solvent outflow and film shrinkage during phase separation. Nevertheless, a consistently high porosity (around 80%) was observed for all membranes. Furthermore, the membranes displayed similar Au contents (6.0–6.4 wt%, determined *via* quantitative EDX) and loadings (140–170 μg cm^{-2}). This corresponds to an exceptionally high AuNP yield of 93–99% (amount Au immobilized in the final membranes compared to amount added as $AuCl_4^-$ to the casting solutions). While copper could not be reliably quantified by EDX due to its low content, the theoretical Cu loading is approximately 5 μg cm^{-2} for all membranes, which we verified exemplarily for the $AuCuPVP_{3Red}$ membrane *via* copper leaching (see SI, Section S9).

3.3 Characterization of gold-decorated membranes

SEM and EDX were used to examine the membrane morphology and the spatial distribution of the immobilized AuNPs (Fig. 2). The membranes exhibit an anisotropic cross-section characteristic of NIPS,[25,26] featuring small finger-like pores near the top surface (exposed first to the water precipitation bath, *cf.* Section 2.2) that transition into larger macrovoids towards the bottom (Fig. 2, middle panels). This structure arises from the kinetics of solvent/non-solvent exchange in the cast polymer solution film after immersion in the water bath, which results in gradual polymer precipitation from top to bottom.

High-resolution SEM images reveal that the AuNPs are primarily located on the internal pore surfaces of the membranes (Fig. 2, left panels), maximizing their accessibility for catalysis (high-resolution EDX mappings are shown in

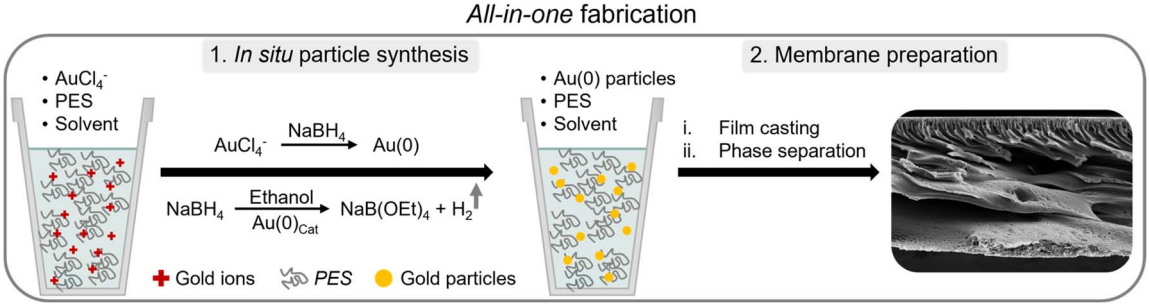

Fig. 1 Schematic depiction of the *all-in-one* fabrication of gold-decorated porous PES membranes. For Cu-doping and PVP capping of AuNPs, Cu^{2+} and PVP were simply added to the casting solution before *in situ* particle synthesis.

 This journal is © The Royal Society of Chemistry 2025

Open Access Article. Published on 28 July 2025. Downloaded on 4/4/2026 4:36:24 PM. This article is licensed under a Creative Commons Attribution 3.0 Unported Licence.

Table 1 Thickness, porosity and Au integration for the prepared gold-decorated membranes

	Thickness [μm]	Porosity [%]	Au content[a] [wt%]	Au loading[b] [μg cm^{-2}]	AuNP yield[c] [%]
Au_{10Red}	93 ± 1	86 ± 2	6.31	157 ± 1	97
$AuCu_{10Red}$	99 ± 7	79 ± 4	6.39	156 ± 3	99
$AuCu_{3Red}$	89 ± 2	78 ± 1	6.17	145 ± 7	95
$AuCu_{1.5Red}$	92 ± 4	83 ± 1	6.02	141 ± 6	93
$AuCuPVP_{3Red}$	107 ± 7	82 ± 4	6.30	168 ± 2	97

[a] Determined *via* quantitative EDX of the membrane cross-section. [b] Calculated based on average membrane density. [c] AuNP yield [%] = solid Au content in membrane [wt%]/dissolved Au precursor content in casting solution [wt% in relation to PES].

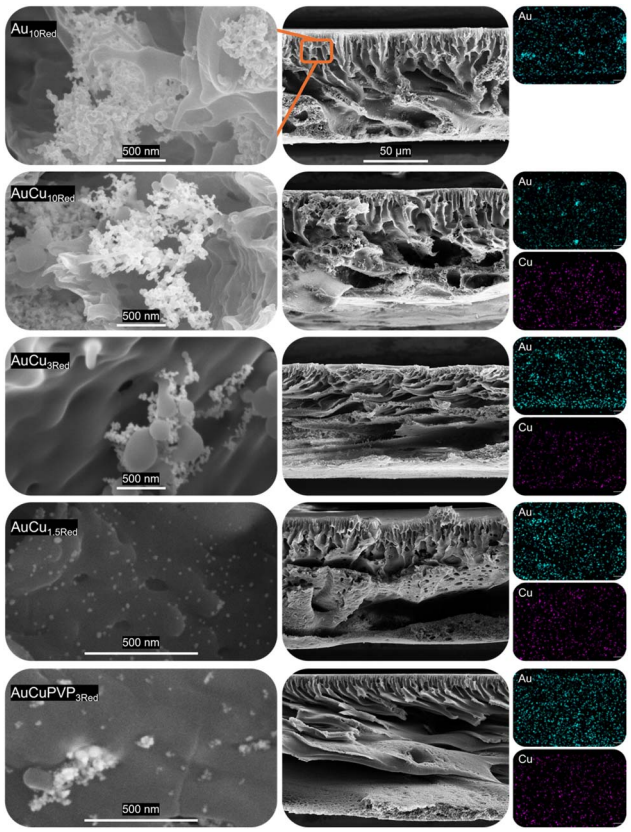

Fig. 2 Exemplary high resolution SEM images of *in situ* formed and subsequently membrane-immobilized AuNPs (left) and SEM images and EDX mapping of the cross-section of all gold-decorated membranes (right). The EDX mappings of Au and Cu correspond to the displayed cross-section. The scale bar shown for Au_{10Red} applies to all cross-section SEM images.

Section S5 of the SI). This preferential location likely occurs during phase separation: as the hydrophobic polymer-rich phase solidifies, the polymer-suspended hydrophilic AuNPs are expelled towards the forming interface with the water-rich (pore-forming) phase, becoming anchored at the pore surface upon final polymer precipitation.

Notably, higher $NaBH_4$ concentrations used during synthesis resulted in poorer nanoparticle dispersion within the membrane, characterized by increased agglomeration. This suggests that a higher ionic strength of the casting solution, resulting from more $NaBH_4$, promotes interaction between *in situ* formed AuNPs.

Membranes prepared with 10 eq. $NaBH_4$ (Au_{10Red}, $AuCu_{10Red}$) showed large particle networks (>500 nm in diameter) composed of numerous primary AuNPs (Fig. 2, left panels). Reducing the $NaBH_4$ amount to 3 eq. ($AuCu_{3Red}$) significantly decreased the extent of agglomeration, while using only 1.5 eq. ($AuCu_{1.5Red}$) resulted in immobilization of individually dispersed nanoparticles. Crucially, the addition of PVP as capping agent during *in situ* synthesis with 3 eq. $NaBH_4$ ($AuCuPVP_{3Red}$) also effectively reduced large-scale agglomeration compared to its PVP-free counterpart ($AuCu_{3Red}$), although some smaller clusters were still formed. As a result, the $AuCuPVP_{3Red}$ membrane features a distribution of AuNPs on its pore surfaces, ranging from individual nanoparticles to small clusters of varying sizes (containing up to ~20 primary particles).

EDX elemental mapping confirmed the presence and co-location of both Au and Cu in the membranes with Cu-doped AuNPs and further demonstrated a relatively homogeneous distribution of nanoparticles throughout the membrane cross-sections (Fig. 2, right panels). Consistent with the SEM images, the EDX maps for membranes prepared with 10 eq. $NaBH_4$ (Au_{10Red} and $AuCu_{10Red}$) clearly showed the presence of large, macroscopic gold agglomerates.

3.4 Particle size and optical properties

The size characteristics of the AuNPs formed *in situ* and the optical properties of both the extracted nanoparticles and the final membranes were investigated (Fig. 3).

To assess the size of the primary nanoparticles immobilized within the membranes, pieces of the gold-decorated membranes were dissolved in NMP, and the resulting dispersions were analysed by DLS (Fig. 3a). This analysis revealed that the apparent solvated diameter (d_{Max}) of the extracted Cu-doped AuNPs decreased significantly from 51 to 26 and 5 nm as the $NaBH_4$ concentration used for *in situ* synthesis was lowered from 10 eq. to 3 eq. and 1.5 eq., respectively. This inverse relationship between reductant concentration and final particle size deviates from the classical LaMer model and suggests an autocatalytic growth mechanism.[41,42] In this scenario, initially formed Au(0) nuclei act as catalytic sites for the reduction and subsequent deposition of further $AuCl_4^-$ from solution. Consequently, higher $NaBH_4$ concentrations lead to faster growth rates and larger final nanoparticles. The trend of decreasing particle size (from 51 to 26 to 5 nm) also correlates

Open Access Article. Published on 28 July 2025. Downloaded on 4/4/2026 4:36:24 PM.
This article is licensed under a Creative Commons Attribution 3.0 Unported Licence.

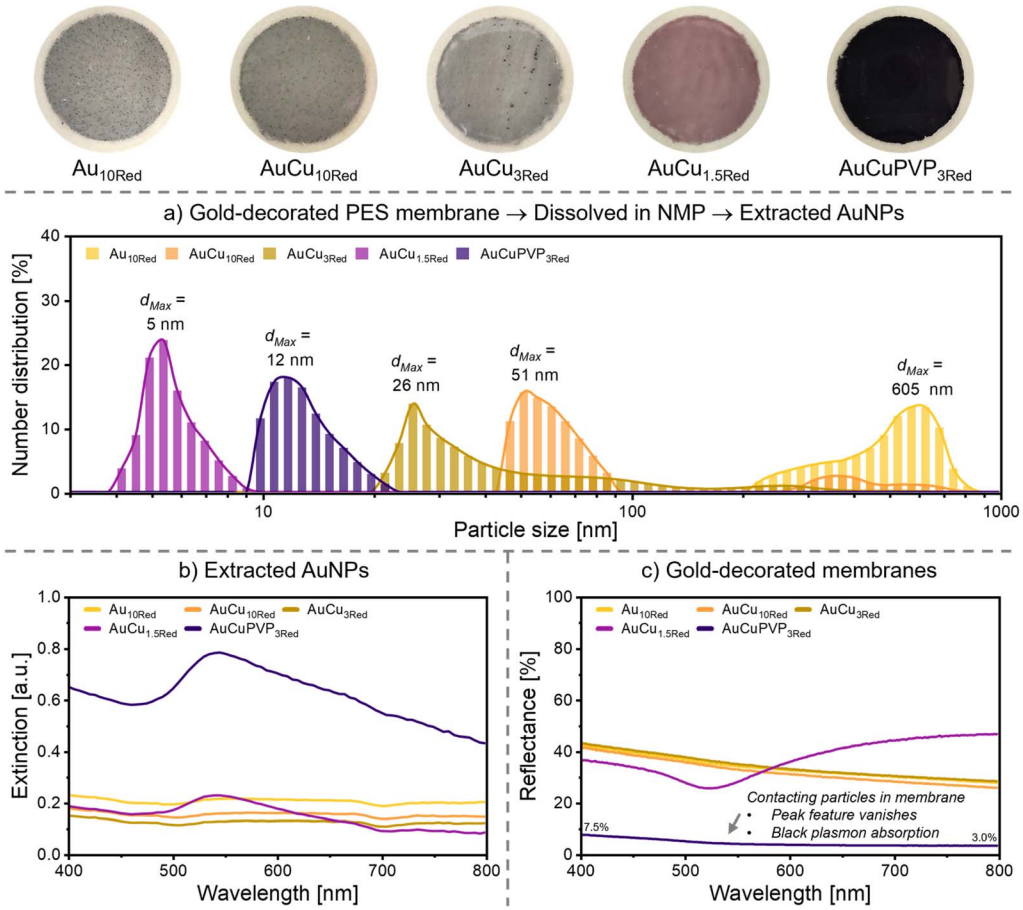

Fig. 3 (a) DLS analysis of dispersed AuNPs extracted from the gold-decorated membranes by dissolution in NMP. (b) UV-Vis extinction of dispersed AuNPs extracted from the gold-decorated membranes by dissolution in NMP. (c) Relative diffuse reflectance (integrating sphere with barium sulfate as white reference) of the gold-decorated membranes (in dry state).

with a slight decrease in AuNP yield for the corresponding membranes: from 99% for $AuCu_{10Red}$ to 95% for $AuCu_{3Red}$ and 93% for $AuCu_{1.5Red}$ (*cf.* Table 1). Since we observed full conversion of all metal precursors in the casting solutions (see SI, Section S4), this gold loss suggests that some smaller particles may diffuse into the water phase before polymer precipitation during membrane fabrication.

Interestingly, although SEM revealed large particle networks (>500 nm) in the intact $AuCu_{10Red}$ membrane (*cf.* Fig. 2), DLS analysis showed that most of the Cu-doped AuNPs extracted from it exhibit much smaller diameter (51 nm), with only a minor particle population in the 300–700 nm range (Fig. 3a). This indicates that the large-scale agglomeration of the Cu-doped AuNPs observed inside the membranes is physical (*e.g.*, van der Waals forces) and reversible. In stark contrast, the non-doped AuNPs from the Au_{10Red} membrane remained irreversibly agglomerated after extraction (d_{Max} = 605 nm). This could be attributed to the sintering of pure AuNPs. Sintering, the irreversible fusion of AuNPs, requires an identical atomic arrangement at the point of contact. Integrating copper atoms may introduces surface heterogeneities that hinder the fusion process.[43]

Adding PVP during the synthesis with 3 eq. $NaBH_4$ ($AuCuPVP_{3Red}$) also effectively limited the nanoparticle growth rate, resulting in extracted nanoparticles with an apparent diameter of 12 nm, significantly smaller than those from $AuCu_{3Red}$ (26 nm). Additionally, PVP-capping promoted a more homogeneous particle growth, yielding a narrow size distribution (10–20 nm). In contrast, for the $AuCu_{3Red}$ membrane we observed a broad distribution with tailing towards 100 nm.

UV-Vis extinction spectra of the nanoparticles extracted and dispersed in NMP correlate well with the DLS and SEM observations (Fig. 3b). Nanoparticles from membranes synthesized with higher $NaBH_4$ amounts or without PVP (Au_{10Red}, $AuCu_{10Red}$, $AuCu_{3Red}$) exhibited low intensity broadband extinction lacking distinct LSPR peaks. This can be attributed to their wide size distribution, which extensively broadens the LSPR spectral range, and their partial agglomeration, which leads to a lower total extinction cross-section due to shadowing effects.[44] Conversely, the narrow-sized Cu-doped AuNPs extracted from the $AuCu_{1.5Red}$ and $AuCuPVP_{3Red}$ membranes displayed distinct LSPR peaks centered around 540 nm and 545 nm, respectively, characteristic of small gold nanoparticles in NMP.[45]

 This journal is © The Royal Society of Chemistry 2025

Open Access Article. Published on 28 July 2025. Downloaded on 4/4/2026 4:36:24 PM.
This article is licensed under a Creative Commons Attribution 3.0 Unported Licence.

Relative diffuse reflectance (*cf.* Section 2.3) of the intact gold-decorated membranes revealed distinct optical properties (Fig. 3c). The $AuCu_{1.5Red}$ membrane, decorated with individually dispersed nanoparticles (*cf.* Fig. 2), showed a reflectance minimum around 525 nm, relatively close to the LSPR peak position of its extracted nanoparticles (the difference can be attributed to air as medium). Strikingly, the $AuCuPVP_{3Red}$ membrane displayed very low diffuse reflectance (between 7.5% and 3.0%) across the entire visible spectrum (400–800 nm), effectively acting as a 'black' plasmonic absorber.[46] This strong broadband absorption, which differs from the behaviour of the extracted nanoparticles, is attributed to the collective plasmonic response of the PVP-capped Cu-doped AuNP population within the membrane's porous polymer matrix (*cf.* Fig. 2).[47] Specifically, the immobilized particle nanoclusters retain a high extinction cross-section, while their varying sizes and interparticle distances lead to plasmon coupling with a wide distribution of coupling strengths.[48] This coupling shifts the plasmon resonances relative to the intrinsic LSPR of the individual particles, creating a superposition of absorption peaks that result in near-continuous and intense visible-light absorption. Importantly, $AuCuPVP_{3Red}$ retained its black absorption after the Cu-dopant was selectively leached from the membrane (see SI, Section S9), demonstrating that plasmonic gold is responsible for this property.

'Black gold' has recently attracted significant interest for catalysis in energy and environmental applications. However, previously reported synthesis procedures are often complex and multi-step (*e.g.*, AuNP growth on supports), designed to generate the necessary plasmonic coupling in powder composites.[49,50] In contrast, the novel, *all-in-one* method presented here provides an efficient and straightforward synthesis of tailored black gold materials, markedly improving material economy and reducing preparation time compared to existing techniques.

3.5 Catalytic degradation of ofloxacin

The catalytic performance of the prepared membranes was evaluated for the degradation of ofloxacin (OFL) in water *via* peroxymonosulfate (PMS) activation in both batch and flow-through modes (Fig. 4). OFL was chosen as an exemplary contaminant due to being one of the antibiotics of emerging concern listed on the 4th Watch List of the EU's water framework directive.

We quantified OFL removal from water based on the decrease in the integrated area of its characteristic UV-Vis peak at 293 nm (π–π^* transition of the aromatic quinolone core) (see SI, Section S2). Although we also evaluated HPLC analysis for quantifying OFL degradation (see SI, Fig. S7), it showed a more rapid removal of the parent compound than the aromatic content measured by UV-Vis. Therefore, UV-Vis was selected as the more relevant method for assessing overall remediation performance, as it also accounts for the degradation of aromatic oxidation intermediates.

As shown in Fig. 4, the Cu-doped membrane ($AuCu_{10Red}$) demonstrated consistently higher catalytic OFL degradation rates than the gold-only membrane (Au_{10Red}). This difference in catalytic activity matched their OFL adsorption rate: Au_{10Red} exhibited substantially lower adsorption than $AuCu_{10Red}$ (3 *vs.* 6 μg OFL per mg metal per h in DI water; 0.5 *vs.* 2 μg mg^{-1} h^{-1} in ion matrix; Fig. 4a). Given that Cu-doping was observed to drastically reduce irreversible nanoparticle agglomeration (*cf.* Fig. 3a), these findings collectively suggest that copper enhances performance by improving the surface accessibility of the membrane-immobilized AuNPs, not by acting as a catalyst itself.

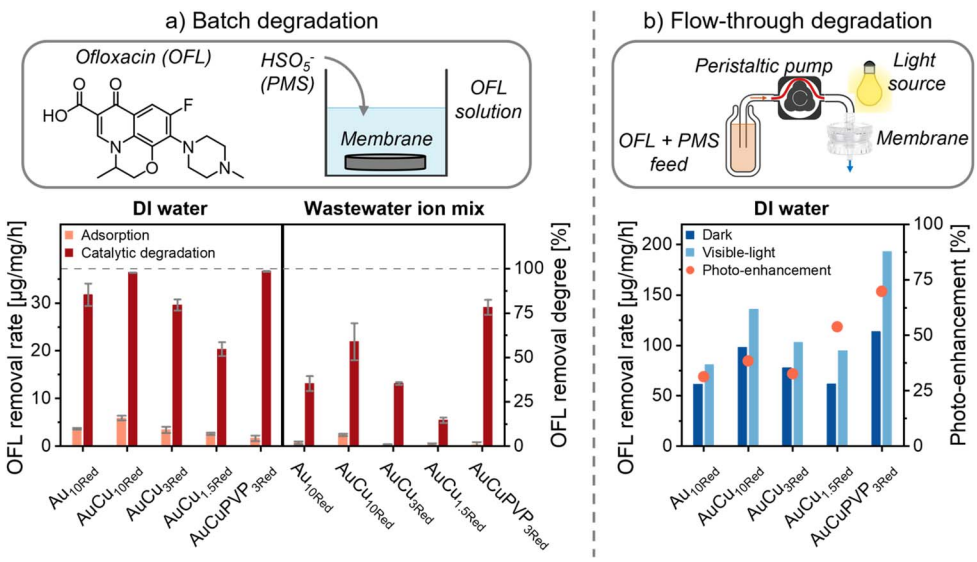

Fig. 4 Performance of gold-decorated membranes in the catalytic degradation of OFL (5 mg L^{-1}) with PMS (0.5 mM). (a) Batch (10 mL) adsorption (without PMS) and degradation (with PMS) of OFL in DI water and a wastewater ion mix (see SI, Section S6). Membranes (2 cm^2) were immersed in the reaction solution and OFL removal was measured after 2 h. (b) Flow-through degradation in DI water using membranes (3 cm^2) as microreactors (100 L m^{-2} h^{-1} flux, dead-end single-pass mode). After 90 min equilibration with the feed (OFL and PMS), OFL removal was determined in permeate collected over 30 min in dark and under visible-light irradiation (>420 nm, 80 mW cm^{-2}) (see SI, Section S8).

Open Access Article. Published on 28 July 2025. Downloaded on 4/4/2026 4:36:24 PM. This article is licensed under a Creative Commons Attribution 3.0 Unported Licence.

In the batch configuration in DI water (Fig. 4a, left), OFL removal by the membranes strongly correlated with the size of the immobilized Cu-doped AuNPs (and thus, $NaBH_4$ concentration used for *all-in-one* synthesis). Decreasing the $NaBH_4$ amount from 10 eq. ($AuCu_{10Red}$, 51 nm) to 3 eq. ($AuCu_{3Red}$, 26 nm) and 1.5 eq. ($AuCu_{1.5Red}$, 5 nm) led to a significant decrease in both the OFL adsorption rate (from 6 to 4 to 3 μg mg^{-1} h^{-1}) and the catalytic degradation rate of OFL with PMS (from 36 to 29 to 20 μg mg^{-1} h^{-1}).

This inverse relationship between OFL adsorption/degradation and geometric surface area (smaller particles yield higher area) suggests that the intrinsic surface properties of smaller AuNPs hinder binding of OFL, a trend that was similarly reported in literature for adsorption of biomolecules.[51] We hypothesize that the higher surface energy of smaller particles may promote the formation of a more strongly bound hydration layer in aqueous solution, a barrier that OFL must displace to bind to the catalyst.

$AuCuPVP_{3Red}$ (12 nm particles, 3 eq. $NaBH_4$, PVP-capped) diverged from the size-dependent activity trend and reached a catalytic OFL degradation rate of 37 μg mg^{-1} h^{-1}. Crucially, this membrane still exhibited a similarly low OFL adsorption as $AuCu_{1.5Red}$ (uncapped 5 nm particles). This suggests the PVP-capped nanoparticles have higher PMS activation activity, compensating the low OFL adsorption. We attribute this enhanced activation to the known effect of PVP of increasing the electron density of AuNPs *via* its electron-donating functional groups (*e.g.*, nitrogen/oxygen lone pairs).[52] This modification may facilitate the non-radical PMS activation pathway known for noble metals like gold.[15] Specifically, donation of electron density from the gold surface to the antibonding orbital (σ*) of the O–O bond of PMS can weaken this bond, promoting its cleavage and the subsequent formation of catalyst-bound non-radical active species.

Conducting the batch degradation experiments in an ion matrix representative of wastewater (including Na^+, K^+, Ca^{2+}, Mg^{2+}, NH_4^+, Cl^-, CO_3^{2-}, PO_4^{3-}; exact composition in SI, Section S6) yielded similar activity trends among the membranes as in DI water (Fig. 4a, right), although OFL adsorption and degradation levels were lower. This indicates that OFL and PMS compete with dissolved ions for active sites on the membrane-immobilized AuNPs. The $AuCuPVP_{3Red}$ membrane demonstrated the modest catalytic rate decrease in the ion matrix (only from 37 to 30 μg mg^{-1} h^{-1}), while its decrease in OFL adsorption was similar to that of the other membranes. This aligns with our hypothesis that PVP capping promotes interaction between the AuNPs and PMS, enhancing the resilience to interference by components of the water matrix. Crucially, we measured the amount of metal ions that leached from the membranes into solution after 2 h batch reaction (see SI, Section S7). All membranes proved highly stable, exhibiting negligible gold (<0.2%) and copper loss (<0.6%).

Visible-light irradiation in continuous flow-through mode further induced photo-enhancement in all membranes (Fig. 4b, see Section S8 in the SI for full Experimental data). The three grey membranes (Au_{10Red}, $AuCu_{10Red}$, $AuCu_{3Red}$) showed similar, moderate enhancement (~35%), suggesting minimal influence of Cu-doping on the photo-response of the immobilized AuNPs. Conversely, $AuCu_{1.5Red}$ and $AuCuPVP_{3Red}$ exhibited significantly larger enhancements of 54% (62 to 95 μg mg^{-1} h^{-1}) and 70% (114 to 194 μg mg^{-1} h^{-1}), respectively. The substantial photo-enhancement in $AuCu_{1.5Red}$, which has a defined LSPR peak (*cf.* Fig. 3c) but the lowest dark activity, strongly points towards plasmon-mediated photocatalysis as enhancement mechanism.

Furthermore, the superior photocatalytic performance of the black gold-decorated $AuCuPVP_{3Red}$ membrane can likely be attributed to its ability to harvest virtually all light across the entire visible spectrum.

To rule out direct photolysis of OFL or PMS, control experiments were conducted in flow-through with a metal-free PES-PVP membrane and also without any membrane (see SI, Section S8). These controls showed no significant PMS-mediated OFL degradation under either dark or light conditions, confirming the essential catalytic function of the gold-decorated membranes. Furthermore, copper was selectively leached from an $AuCuPVP_{3Red}$ sample using HCl (see SI, Section S9), which did neither reduce the catalytic OFL removal rate of this membrane nor its photo-enhancement effect. This demonstrates that copper does not significantly contribute to the catalytic performance of the AuNPs. Instead, its primary role is to control the AuNP formation during the *in situ* synthesis. Finally, to assess the role of photo-heating, the surface temperature of $AuCuPVP_{3Red}$ was measured under visible-light irradiation (see SI, Section S10), revealing an increase of only 2 °C in static conditions. This indicates that the 70% photo-enhancement observed for this membrane is dominated by photocatalytic effects, with only a minor contribution of photo-heating.

3.6 Impact of flow-through process parameter

Next, we evaluated key parameters affecting the flow-through catalytic performance of the $AuCuPVP_{3Red}$ membrane for OFL degradation with PMS under visible-light irradiation (Fig. 5). Adjusting the flux allowed variation of the residence time (τ) in the membrane (Fig. 5a, left). The flow-through degradation exhibits pseudo-first-order kinetics ($[OFL] = [OFL]_0\, e^{-k\tau}$) relative to OFL, as PMS was supplied in excess. Single-pass OFL removal showed strong exponential dependence on τ, rising from approximately 20% at $\tau = 1$ s to over 95% at $\tau = 9$ s. This yields an apparent rate constant (k) of 0.27 s^{-1}, underscoring the high photocatalytic PMS activation and OFL oxidation activity of the black gold membrane. The initial OFL concentration ($[OFL]_0$) also influenced relative removal (Fig. 5a, right), albeit less strongly than τ. Decreasing $[OFL]_0$ from 5 mg L^{-1} to 3 mg L^{-1} resulted in only a 6% increase in single-pass removal degree. While the ratio of catalyst sites to OFL molecules increases at lower $[OFL]_0$ (favouring complete reaction), the absolute conversion rate simultaneously decreases due to the pseudo-first-order kinetics, leading to only slightly higher relative OFL removal efficiency. However, the impact of catalyst site availability becomes dominant at very low concentrations. At 0.75 mg L^{-1} OFL, near-complete removal (~99%) was achieved

 This journal is © The Royal Society of Chemistry 2025

Open Access Article. Published on 28 July 2025. Downloaded on 4/4/2026 4:36:24 PM.
This article is licensed under a Creative Commons Attribution 3.0 Unported Licence.

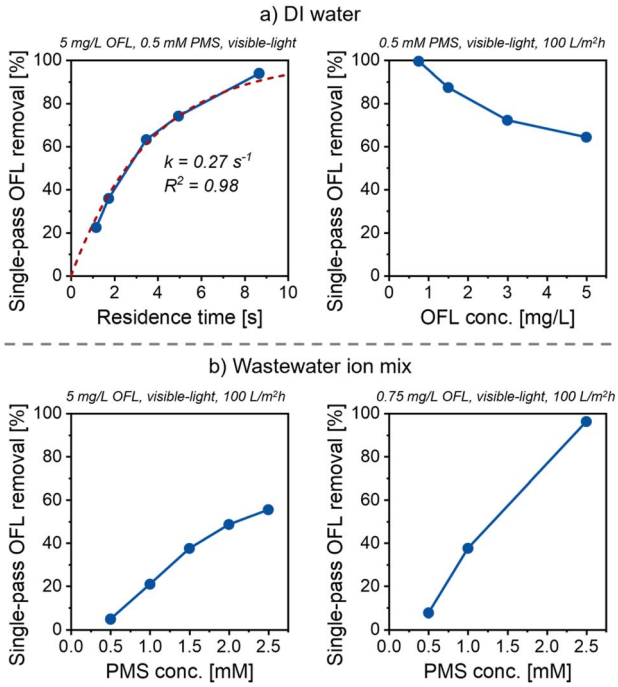

Fig. 5 Impact of process parameter on the performance of the AuCuPVP$_{3Red}$ membrane (3 cm^2, single-pass dead-end mode) in the photocatalytic flow-through degradation of OFL with PMS under visible-light irradiation (80 mW cm^{-2}). (a) Variation of residence time and of OFL concentration in DI water. (b) Variation of PMS concentration for different OFL concentrations in wastewater ion mix. Each experiment was conducted with a new membrane sample.

in single-pass, indicating that catalyst sites in the membrane were sufficiently abundant relative to OFL molecules under these conditions.

In the presence of the wastewater ion mix, competitive adsorption between PMS and dissolved anions onto the AuNPs became limiting for PMS activation and OFL removal (Fig. 5b). Consequently, increasing the PMS concentration from 0.5 mM (yielding ~5% OFL removal) sharply increased performance by promoting PMS adsorption. Saturation began around 2.0–2.5 mM PMS, indicating that at higher PMS levels, the intrinsic photocatalytic turnover rate of the gold catalyst, rather than PMS binding, limits OFL oxidation. Under these conditions (ion mix, 2.5 mM PMS), single-pass removal was ~55% for $[OFL]_0$ = 5 mg L^{-1}. However, targeting a more environmentally relevant concentration, the membrane demonstrated exceptional efficiency: ~99% OFL removal was achieved at $[OFL]_0$ = 0.75 mg L^{-1} with the complex ion water matrix and a residence time of only 3.5 s in the AuCuPVP$_{3Red}$ membrane.

3.7 Photocatalytic mechanism of PMS activation

The (photo)catalytic PMS activation pathway was investigated in flow-through experiments with the AuCuPVP$_{3Red}$ membrane using selective active species probes (Fig. 6): benzoic acid (BA), 4-hydroxybenzoic acid (HBA), and nitro blue tetrazolium (NBT). While BA and HBA both react with $^{\bullet}SO_4^-$ at similar rates, HBA reacts approximately twice as fast with $^{\bullet}OH$ compared to BA.[53,54]

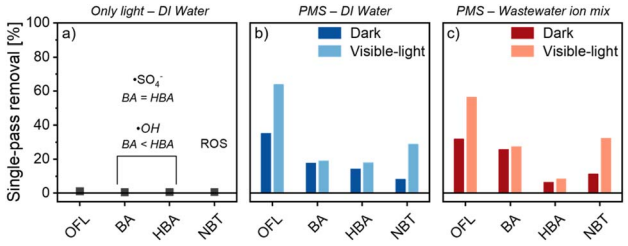

Fig. 6 Elucidation of photocatalytic PMS activation mechanism of AuCuPVP$_{3Red}$. Single-pass removal efficiencies of OFL and radical probes (5 mg L^{-1} each) were measured in flow-through dead-end mode (100 L m^{-2} h^{-1}). For each experiment a new membrane sample (3 cm^2) was used and first equilibrated for 120 min with OFL feed (see SI, Section S11). (a) Visible-light only (no PMS) in DI water. (b) With PMS (0.5 mM) in DI water in dark and under visible-light irradiation (80 mW cm^{-2}). (c) With PMS (2.5 mM) in wastewater ion mix in dark and under visible-light irradiation (80 mW cm^{-2}).

NBT was used to probe for reactive oxygen species (ROS), specifically $^{\bullet}O_2^-$.[55]

In all experiments, prior to evaluating single-pass removal efficiencies, each AuCuPVP$_{3Red}$ sample was first equilibrated with an OFL solution for 120 min under flow-through conditions to saturate their adsorption capacity (see Section S11 in the SI for full Experimental data). Under visible-light irradiation but in the absence of PMS, virtually no removal of OFL and the three probe molecules was observed (Fig. 6a). This confirms that the membrane-immobilized black plasmonic AuNPs cannot photocatalytically generate active species directly from water or dissolved oxygen (*e.g.*, $O_2 + e^- = {}^{\bullet}O_2^-$ and $OH^- + h^+ = {}^{\bullet}OH$ does not occur).

Under dark conditions with PMS present, flow-through OFL removal significantly exceeded that of the probe molecules in both DI water and the wastewater ion mix (Fig. 6b and c). As for OFL, the removal efficiencies of the probe molecules reflect their extent of aromatic oxidation, determined by the decrease in their characteristic aromatic absorption peaks (see SI, Section S2). While BA, HBA and NBT react readily with radicals ($^{\bullet}OH$, $^{\bullet}SO_4^-$, $^{\bullet}O_2^-$), their electrochemical redox potentials are relatively high due to their electron-deficient aromatic systems, implying that they are less susceptible to non-radical oxidation.[56] Conversely, OFL features electron-donating nitrogen and oxygen heteroatoms (*cf.* Fig. 4), creating an electron-rich aromatic system that can be oxidized more easily.

This suggests that the AuNPs catalyse a non-radical PMS activation pathway under dark conditions. This non-radical mechanism is further supported by the relation between BA and HBA degradation. In DI water, their removal efficiencies were similar (Fig. 6b), whereas in the wastewater ion mix, BA was degraded more efficiently (Fig. 6c). This pattern contradicts their theoretical radical reactivity, as $^{\bullet}SO_4^-$ should degrade both similarly and $^{\bullet}OH$ should preferentially degrade HBA over BA.[53,54]

Therefore, we propose a surface-mediated mechanism initiated by the adsorption of PMS onto gold (eqn (1)). Electron density is shifted from the catalyst to the σ* orbital of the O–O group of PMS, which promotes its non-radical cleavage and yields an Au–oxygen intermediate (eqn (2)). Subsequently, this

Open Access Article. Published on 28 July 2025. Downloaded on 4/4/2026 4:36:24 PM.
This article is licensed under a Creative Commons Attribution 3.0 Unported Licence.

surface-activated oxygen is transferred to co-adsorbed organic molecules, facilitating the oxidation of the latter (eqn (3)).

$$Au + HO–O–SO_3^- = Au–OH–O–SO_3^- \quad (1)$$

$$Au–OH–O–SO_3^- = Au–O^* + SO_4^{2-} + H^+ \quad (2)$$

$$Au–O^* + organics = Au + O\text{-}organics \quad (3)$$

Visible-light irradiation of the AuCuPVP$_{3Red}$ membrane in presence of PMS resulted in photo-enhancement of the PMS-mediated oxidation of OFL and NBT, without affecting the removal of BA or HBA (Fig. 6b and c). This probe molecule selectivity implies that the immobilized black AuNPs generate specific active species *via* plasmonic photocatalysis, instead of unselectively enhancing conversion through photo-heating. Furthermore, published rate constants show that while NBT reacts with $^{\bullet}O_2^-$, $^{\bullet}SO_4^-$ and $^{\bullet}OH$, both BA and HBA react readily only with $^{\bullet}SO_4^-$/$^{\bullet}OH$.[53–55] Therefore, we can deduce that $^{\bullet}O_2^-$ was generated as an active species under visible-light irradiation. Additionally, the fact that photocatalytic activity was only observed in the presence of PMS (*cf.* Fig. 6a) suggests that $^{\bullet}O_2^-$ is generated *via* a PMS-mediated pathway.

Based on these findings, we propose that the Au–oxygen intermediates generated from PMS (*via* eqn (2)) can migrate and form surface-bound dimers (eqn (4)). Subsequently, the black gold catalyst may transfer a 'hot' electron from photo-excited LSPR to the dimer, releasing $^{\bullet}O_2^-$ (eqn (5)).

$$2\ Au–O^* = Au + Au–O^*–^*O \quad (4)$$

$$Au–O^*–^*O + h\nu = Au^+ + {}^{\bullet}O_2^- \quad (5)$$

Notably, while Au^+ generation from Au(0) under light irradiation is known,[57] it faces a significant thermodynamic barrier due to the high redox potential of Au(0). However, sulfur-containing compounds (*e.g.*, HSO_5^-) exhibit a strong affinity for gold and can stabilize the Au^+ state, lowering the effective energy barrier for its formation.[58,59] This suggests that HSO_5^- may additionally act as photosensitizer, promoting photo-induced electron release from gold by stabilizing Au^+. Importantly, we further measured whether metal leached from the AuCuPVP$_{3Red}$ membrane during the photocatalytic flow-through process (*via* atomic absorption spectroscopy, *cf.* Section S7 in the SI). The combined PMS/illumination treatment in both DI water and wastewater ion mix caused a negligible initial leaching (first 30 min permeate with 15 mL: ≤0.02 mg L^{-1} Cu, ≤2% loss; ≤0.1 mg L^{-1} Au, ≤0.3% loss), with levels dropping below the detection limit (<0.005 mg L^{-1}) in permeates collected after 30 min flow-through. These results show that the proposed transient formation of Au^+ does not cause any significant gold loss, possibly due to rapid regeneration of the Au(0) state *via* substrate oxidation (*e.g.*, OFL/NBT).

3.8 Continuous catalytic water treatment

Finally, we evaluated the continuous water treatment performance of the AuCuPVP$_{3Red}$ membrane in the photocatalytic and PMS-mediated OFL degradation (Fig. 7). For this, water contaminated with 0.75 mg L^{-1} OFL (feed) was continuously pumped through the membrane and the OFL removal from the permeate was monitored after single-pass; the permeate thus represents the final treated effluent that would be directly released during practical application of this process.

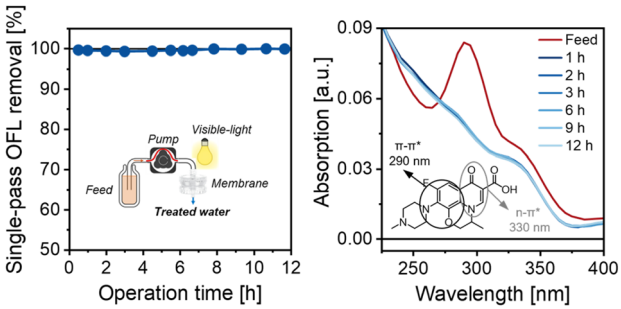

Fig. 7 Continuous treatment of OFL contaminated water (0.75 mg L^{-1}) *via* photocatalytic (80 mW cm^{-2}) and PMS-mediated (0.5 mM) oxidation in flow-through (100 L^{-1} m^{-2} h^{-1}) using the AuCuPVP$_{3Red}$ membrane (3 cm^2).

AuCuPVP$_{3Red}$ maintained virtually complete OFL removal (>99%) over 12 h of continuous operation, processing a total volume of 1200 L m^{-2} (Fig. 7, left). This was achieved despite a short residence time within the membrane of approximately 3.5 s.

Analysis of the permeate's UV-Vis spectra provided additional insight into the degradation process (Fig. 7, right). While the characteristic OFL peak at 290 nm (π–π* transition, conjugated aromatic system) disappeared completely, absorbance at shorter wavelengths (<270 nm) increased slightly. Furthermore, the weaker absorption shoulder around 330 nm, associated with n–π* transitions involving the enone moiety, decreased less significantly. This suggests that while the parent OFL was effectively destroyed, degradation byproducts that still contain the enone moiety are less readily oxidized under these conditions and persist in the treated effluent.

Nevertheless, achieving sustained, near-complete oxidation of the fluoroquinolone core, which is responsible for OFL's antibiotic activity, highlights the exceptional catalytic performance of the AuCuPVP$_{3Red}$ membrane. The potential of this membrane is further underscored by comparing its performance to other reported catalytic membranes for micropollutant degradation (see SI, Section S12).[36,60–64] The maximum calculated turnover frequency (TOF) for OFL degradation by our black gold-decorated AuCuPVP$_{3Red}$ membrane reached approximately 105 × 10^{-3} h^{-1} (mol OFL per mol catalyst per h), significantly exceeding the TOFs reported for other membranes by factors ranging from 5 to 100.

While many catalysts developed for oxidative water treatment utilize more abundant and less expensive non-noble metals a review of literature indicates that such non-noble metal-based catalytic membranes often suffer from significant metal leaching during continuous operation, with reported effluent concentrations reaching levels as high as 2 mg L^{-1} for potentially toxic metals like cobalt (see SI, Section S12).[36,60–64]

This journal is © The Royal Society of Chemistry 2025

Open Access Article. Published on 28 July 2025. Downloaded on 4/4/2026 4:36:24 PM.
This article is licensed under a Creative Commons Attribution 3.0 Unported Licence.

This comparison highlights a crucial advantage of the highly stable gold-decorated membranes presented here, which exhibit negligible metal leaching, ensuring effluent quality and long-term stability.

4 Conclusion

This work highlights a powerful strategy for designing advanced catalytic materials, combining a resource-efficient synthesis with tailored plasmonic properties to create robust and highly effective membranes for sustainable water purification. The presented *all-in-one* approach combines *in situ* particle synthesis within the casting solution with immediate particle immobilization during membrane formation *via* film casting and polymer precipitation in water. First, this integrated method achieved exceptionally high immobilized AuNP yields, overcoming the significant material loss that often plagues traditional membrane functionalization approaches like blending or coating. Secondly, the rapid immobilization of AuNPs immediately following their formation could effectively prevent agglomeration, which is a common challenge in conventional synthesis protocols for small nanoparticles.

We further demonstrated that this *all-in-one* method allows for precise control over the effective size (5 to 51 nm) and spatial arrangement of the immobilized AuNPs by tuning reaction conditions (copper doping, $NaBH_4$ concentration, PVP capping). This control enabled the tailoring of plasmonic coupling, culminating in the $AuCuPVP_{3Red}$ membrane with its broadband 'black plasmonic' absorption properties. This black gold membrane with 12 nm PVP-capped AuNPs displayed the best catalytic performance, likely due to a combination of PVP complexation promoting PMS activation and enhanced photocatalytic activity arising from its effective light harvesting. Mechanistic investigations using probe molecules suggested a dual activation pathway involving non-radical surface-mediated PMS activation dominant in the dark, supplemented by plasmon-enhanced generation of superoxide radicals ($^{\bullet}O_2^-$) under illumination. Crucially, the $AuCuPVP_{3Red}$ membrane demonstrated outstanding potential for practical application, achieving >99% single-pass ofloxacin removal in flow-through mode, even in a complex ionic water matrix. Our systems performance surpasses that of other state-of-the-art catalytic membranes from literature, both in catalytic turnover frequency and operational stability.

Author contributions

Janine Gerlach: methodology, investigation, formal analysis, writing – review & editing. Nourman Barakat: methodology, investigation, writing – review & editing. Lukas Fischer: project administration, supervision, conceptualization, methodology, formal analysis, writing – original Draft, visualization, funding acquisition.

Conflicts of interest

There are no conflicts to declare.

Data availability

Materials; quantification of organic solute removal; metal precursor conversion; high-resolution SEM and EDX analysis; composition of ionic water matrix; metal leaching quantification; experimental data of all flow-through experiments; comparison with data from literature. The data supporting this article have been included as part of the SI.

Supplementary information is available. See DOI: **https://doi.org/10.1039/d5ta03185k**.

Acknowledgements

Dr Lukas Fischer is grateful for the funding by the Deutsche Forschungsgemeinschaft (DFG, German Research Foundation – grant 530864107), with which this research was financed. The authors further thank Tobias Bochmann and Robin Meya, both at UDE, for conducting the SEM and AAS measurements, respectively.

References

1 S. Thanigaivel, S. Vickram, N. Dey, P. Jeyanthi, R. Subbaiya, W. Kim, M. Govarthanan and N. Karmegam, *Chemosphere*, 2023, **313**, 137475.
2 D.-P. Häder, A. T. Banaszak, V. E. Villafañe, M. A. Narvarte, R. A. González and E. W. Helbling, *Sci. Total Environ.*, 2020, **713**, 136586.
3 K. C. Jones, *Environ. Sci. Technol.*, 2021, **55**, 9400–9412.
4 D. G. J. Larsson and C.-F. Flach, *Nat. Rev. Microbiol.*, 2022, **20**, 257–269.
5 A. Saravanan, P. Senthil Kumar, S. Jeevanantham, S. Karishma, B. Tajsabreen, P. R. Yaashikaa and B. Reshma, *Chemosphere*, 2021, **280**, 130595.
6 J. Aravind kumar, T. Krithiga, S. Sathish, A. A. Renita, D. Prabu, S. Lokesh, R. Geetha, S. K. R. Namasivayam and M. Sillanpaa, *Sci. Total Environ.*, 2022, **831**, 154808.
7 D. Ma, H. Yi, C. Lai, X. Liu, X. Huo, Z. An, L. Li, Y. Fu, B. Li, M. Zhang, L. Qin, S. Liu and L. Yang, *Chemosphere*, 2021, **275**, 130104.
8 I. A. Ike, K. G. Linden, J. D. Orbell and M. Duke, *Chem. Eng. J.*, 2018, **338**, 651–669.
9 S. Wu, L. Shen, Y. Lin, K. Yin and C. Yang, *Chem. Eng. J.*, 2021, **414**, 128872.
10 J. Han, L. Sun, M. Ulbricht, L. Fischer, G. Zhang, W. Gao, L. Lv, T. Ren, X. Liu and Z. Ren, *Chem. Eng. J.*, 2025, **505**, 159084.
11 J. Leichtweis, E. Carissimi, U. Hagemann, M. Ulbricht and L. Fischer, *Chem. Eng. J.*, 2023, **477**, 147203.
12 J. Leichtweis, Y. Vieira, E. Carissimi, M. Ulbricht and L. Fischer, *Appl. Surf. Sci.*, 2024, **669**, 160603.
13 Y. Lei, C.-S. Chen, Y.-J. Tu, Y.-H. Huang and H. Zhang, *Environ. Sci. Technol.*, 2015, **49**, 6838–6845.
14 T. Yu, H. Chen, T. Hu, J. Feng, W. Xing, L. Tang and W. Tang, *Appl. Catal., B*, 2024, **342**, 123401.
15 Y.-Y. Ahn, E.-T. Yun, J.-W. Seo, C. Lee, S. H. Kim, J.-H. Kim and J. Lee, *Environ. Sci. Technol.*, 2016, **50**, 10187–10197.

Open Access Article. Published on 28 July 2025. Downloaded on 4/4/2026 4:36:24 PM. This article is licensed under a Creative Commons Attribution 3.0 Unported Licence.

16 G. Young Kim, D. Lee, H.-S. Choe, J.-M. Park, S. Jeong, E. Jongwoo Park, J. Won Lee, C. Lee and J.-H. Kim, *Environ. Sci.: Nano*, 2022, **9**, 2510–2520.
17 M. E. King, C. Wang, M. V. F. Guzman and M. B. Ross, *Chem Catal.*, 2022, **2**, 1880–1892.
18 V. Guerrero-Florez, S. C. Mendez-Sanchez, O. A. Patrón-Soberano, V. Rodríguez-González, D. Blach and F. M. O, *J. Mater. Chem. B*, 2020, **8**, 2862–2875.
19 B. C. Hodges, E. L. Cates and J.-H. Kim, *Nat. Nanotechnol.*, 2018, **13**, 642–650.
20 G. Maniakova, K. Kowalska, S. Murgolo, G. Mascolo, G. Libralato, G. Lofrano, O. Sacco, M. Guida and L. Rizzo, *Sep. Purif. Technol.*, 2020, **236**, 116249.
21 X. Zheng, X. Niu, D. Zhang, M. Lv, X. Ye, J. Ma, Z. Lin and M. Fu, *Chem. Eng. J.*, 2022, **429**, 132323.
22 N. Li, X. Lu, M. He, X. Duan, B. Yan, G. Chen and S. Wang, *J. Hazard. Mater.*, 2021, **414**, 125478.
23 J. Liang, K. Gao, A. Zhou, Y. Fang, S. Su, L. Fu, M. Sun and X. Duan, *Appl. Catal., B*, 2023, **327**, 122440.
24 D.-M. Wang and J.-Y. Lai, *Curr. Opin. Chem. Eng.*, 2013, **2**, 229–237.
25 H. Susanto, N. Stahra and M. Ulbricht, *J. Membr. Sci.*, 2009, **342**, 153–164.
26 S. Mazinani, S. Darvishmanesh, A. Ehsanzadeh and B. Van der Bruggen, *J. Membr. Sci.*, 2017, **526**, 301–314.
27 L. Y. Ng, A. W. Mohammad, C. P. Leo and N. Hilal, *Desalination*, 2013, **308**, 15–33.
28 S. S. Ozdemir, M. G. Buonomenna and E. Drioli, *Appl. Catal., A*, 2006, **307**, 167–183.
29 Rajlaxmi, N. Gupta, R. P. Behere, R. K. Layek and B. K. Kuila, *Mater. Today Chem.*, 2021, **22**, 100600.
30 J. Yin and B. Deng, *J. Membr. Sci.*, 2015, **479**, 256–275.
31 D. Radziuk, D. Grigoriev, W. Zhang, D. Su, H. Möhwald and D. Shchukin, *J. Phys. Chem. C*, 2010, **114**, 1835–1843.
32 L. Fischer, A. Volz, U. Hagemann and M. Ulbricht, *Chem. Eng. J.*, 2023, **463**, 142437.
33 L. Fischer, S. A. H. Hesaraki, A. Volz and M. Ulbricht, *ACS Appl. Nano Mater.*, 2023, **6**, 14910–14920.
34 W. Qing, F. Liu, H. Yao, S. Sun, C. Chen and W. Zhang, *Adv. Colloid Interface Sci.*, 2020, **282**, 102207.
35 Z. He, S. Mahmud, Y. Yang, L. Zhu, Y. Zhao, Q. Zeng, Z. Xiong and S. Zhao, *Sep. Purif. Technol.*, 2020, **250**, 117266.
36 Y. Bao, W. J. Lee, T.-T. Lim, R. Wang and X. Hu, *Appl. Catal., B*, 2019, **254**, 37–46.
37 I. Sanjuán, V. Kumbhar, O. Prymak, M. Ulbricht, C. Andronescu and L. Fischer, *ChemSusChem*, 2025, **18**, e202401228.
38 S. A. H. Hesaraki, O. Prymak, M. Heidelmann, M. Ulbricht and L. Fischer, *ACS Appl. Mater. Interfaces*, 2024, **16**, 17517–17530.
39 S. A. H. Hesaraki, M. Ulbricht and L. Fischer, *Chem. Eng. J.*, 2024, **498**, 155266.
40 M. Ropertz, M. Ulbricht and L. Fischer, *Chem. Eng. J. Adv.*, 2024, **20**, 100683.
41 C. B. Whitehead, M. A. Watzky and R. G. Finke, *J. Phys. Chem. C*, 2020, **124**, 24543–24554.
42 P. N. Njoki, J. Luo, M. M. Kamundi, S. Lim and C.-J. Zhong, *Langmuir*, 2010, **26**, 13622–13629.
43 E. S. Gnanakumar, J. M. Naik, M. Manikandan, T. Raja and C. S. Gopinath, *ChemCatChem*, 2014, **6**, 3116–3124.
44 J. M. Zook, V. Rastogi, R. I. MacCuspie, A. M. Keene and J. Fagan, *ACS Nano*, 2011, **5**, 8070–8079.
45 X. Liu, M. Atwater, J. Wang and Q. Huo, *Colloids Surf., B*, 2007, **58**, 3–7.
46 Y. Liu, Z. Liu, Q. Huang, X. Liang, X. Zhou, H. Fu, Q. Wu, J. Zhang and W. Xie, *J. Mater. Chem. A*, 2019, **7**, 2581–2588.
47 K. Bae, G. Kang, S. K. Cho, W. Park, K. Kim and W. J. Padilla, *Nat. Commun.*, 2015, **6**, 10103.
48 E. Ringe, M. R. Langille, K. Sohn, J. Zhang, J. Huang, C. A. Mirkin, R. P. Van Duyne and L. D. Marks, *J. Phys. Chem. Lett.*, 2012, **3**, 1479–1483.
49 D. Liu, F. Zhou, C. Li, T. Zhang, H. Zhang, W. Cai and Y. Li, *Angew. Chem., Int. Ed.*, 2015, **54**, 9596–9600.
50 R. Verma, S. Kundu and V. Polshettiwar, *J. Mater. Chem. A*, 2024, **12**, 27235–27245.
51 K. Kaur and J. A. Forrest, *Langmuir*, 2012, **28**, 2736–2744.
52 H. Tsunoyama, N. Ichikuni, H. Sakurai and T. Tsukuda, *J. Am. Chem. Soc.*, 2009, **131**, 7086–7093.
53 G. V. Buxton, C. L. Greenstock, W. P. Helman and A. B. Ross, *J. Phys. Chem. Ref. Data*, 1988, **17**, 513–886.
54 P. Neta, R. E. Huie and A. B. Ross, *J. Phys. Chem. Ref. Data*, 1988, **17**, 1027–1284.
55 Y. Wen, J. Yan, B. Yang, Z. Zhuang and Y. Yu, *J. Mater. Chem. A*, 2022, **10**, 19184–19210.
56 P. Luo, E. C. Feinberg, G. Guirado, S. Farid and J. P. Dinnocenzo, *J. Org. Chem.*, 2014, **79**, 9297–9304.
57 Z. Mao, R. Espinoza, A. Garcia, A. Enwright, H. Vang and S. C. Nguyen, *ACS Nano*, 2020, **14**, 7038–7045.
58 S. Witzel, A. S. K. Hashmi and J. Xie, *Chem. Rev.*, 2021, **121**, 8868–8925.
59 U. Koelle and A. Laguna, *Inorg. Chim. Acta*, 1999, **290**, 44–50.
60 S. Wang, J. Tian, Z. Wang, Q. Wang, J. Jia, X. Hao, S. Gao and F. Cui, *Chem. Eng. J.*, 2020, **396**, 125289.
61 A. Liangdy, W. J. Lee, P. Tonanon, R. D. Webster, S. A. Snyder and T.-T. Lim, *Chem. Eng. J.*, 2023, **454**, 140075.
62 W. J. Lee, Y. Bao, A. Liangdy, X. Hu and T.-T. Lim, *Chem. Eng. J.*, 2022, **430**, 132921.
63 S. Sun, H. Yao, W. Fu, S. Xue and W. Zhang, *J. Hazard. Mater.*, 2020, **386**, 121955.
64 J. Liang, K. Gao, A. Zhou, Y. Fang, S. Su, L. Fu, M. Sun and X. Duan, *Appl. Catal., B*, 2023, **327**, 122440.

This journal is © The Royal Society of Chemistry 2025